Eur. Phys. J. E (2012) **35**: 19
DOI 10.1140/epje/i2012-12019-8

THE EUROPEAN PHYSICAL JOURNAL E

Regular Article

Free surface flow between two horizontal concentric cylinders

J. Peixinho[a], P. Mirbod, and J.F. Morris

Benjamin Levich Institute and Department of Chemical Engineering, City College of City University of New York, New York, NY 10031, USA

Received 20 October 2011 and Received in final form 28 February 2012
Published online: 21 March 2012 –

Abstract. Results are reported on a combined experimental and numerical investigation of a free surface flow at small Reynolds numbers. The flow is driven by the rotation of the inner of two horizontal concentric cylinders, with an inner to outer radius ratio of 0.43. The outer cylinder is stationary. The annular gap is partially filled, from 0.5 to 0.95 full, with a viscous liquid leaving a free surface. When the fraction of the annular volume filled by liquid is 0.5, a thin liquid film covers the rotating inner cylinder and reenters the liquid pool. For relatively low rotation speeds, the evolution of the film thickness is consistent with the theory for a plate being withdrawn from an infinite liquid pool. The overall liquid flow pattern at this condition consists of two counter-rotating cells: one is around the inner cylinder and the other with weaker circulation rate is in the bottom part of the annulus and nearly symmetric about the vertical axis. With increasing rotation rate, the free surface becomes more deformed, and the dynamics of the stagnation line and the cusp line dividing the cells are tracked as quantitative measures of the interface shape. In addition, the recirculating flow cells lose symmetry and the cusp deforms the free surface severely. A comparison of numerically computed flow which describes the interface by a phase-field method confirms the dynamics of the two cells and the interface deformation. For filling fraction 0.75, the liquid level is slightly above the inner cylinder and a significant decrease in size of the bottom cell with increasing rotation rate is found. For filling fractions approaching unity, the liquid flow consists of one single cell and the surface deformation remains small.

1 Introduction

The flow of viscous liquids with free surfaces is fundamental in many situations, ranging from surface coating to geophysical flows. Such flows often exhibit interesting phenomena. One example is liquid flow in a partially filled horizontal cylinder, with flow driven by rotating the cylinder about its axis. For this geometry surprising flow patterns due to secondary flows driven by the dragging of a liquid film have been described [1]; later works showed that different flow patterns may arise [2,3]. A related configuration, in which is found a ribbing or printer's instability, is obtained when the gap between two concentric cylinders is slightly filled with liquid. For small but finite velocities, the flow structure in this geometry may show a complicated set of stagnation lines as well as elliptic and hyperbolic stagnation points between the cylinders. This flow exhibits "nested separatrices" and the structure observed is sensitive to the radius ratio and the speed ratio of the cylinders [4]. The topology of these streamlines and their bifurcations can be understood in the framework of dynamical system theory [5], although experimental comparisons are challenging.

In the present investigation, we consider the flow of a viscous liquid in a partially filled annulus between two horizontal concentric cylinders. Flow is driven by rotation of the inner cylinder. The behavior of the free surface and its relation to the subsurface dynamics are studied. While aspects of this problem have been investigated numerically, there remains a lack of quantitative data, particularly on the free surface morphology, which will be shown to exhibit both large-scale surface deformation and cusp formation.

Analysis of the flow we consider is rather limited. However, the Stokes flow in a half-filled annulus between rotating coaxial cylinders was computed by [6]. This work differs from the present study in considering both cylinders to be rotating, which renders direct comparison impossible given our experimental constraints. The liquid in the calculation noted is confined to the bottom of the annulus, *i.e.* the flow is sufficiently slow that gravity dominates and the interface is flat. Surface tension thus never plays a role. In addition, these authors assumed that i) the thicknesses of the films which develop along the surface of the

[a] *Present address*: Laboratoire Ondes et Milieux Complexes, CNRS UMR 6294 et Université du Havre, 53 rue de Prony, 76600 Le Havre, France.
e-mail: jorge.peixinho@univ-lehavre.fr

cylinders are vanishingly small; and, ii) the free surface remains undeformed everywhere except within the immediate neighborhood of the cylinders. While there can be no direct comparison, it is useful to note that under these conditions, for certain parameter ranges they found the flow to consist of two large cells or eddies: one below but connected to the inner cylinder, and the other in the bottom part of the annulus. Depending on the radius ratio and the speed ratio between the cylinders, the circulations have a potentially rich substructure with separatrices and sub-eddies [4], and it has been noted that the realizability of such flows computed assuming a flat interface depends upon the actual shape of the boundary (*i.e.* the interface).

It is the purpose of the present work to determine this interface shape and the sub-surface flow, both experimentally and numerically, for the arrangement described in [6] but with only the inner cylinder rotating. We outline the main results, as the interface shape and its underlying basis in wetting of the driving boundary lead to a flow quite different than one might deduce for a flat interface and no liquid film over the cylinder. We consider a range of fill fractions with $F \geq 0.5$, as well as for a range of capillary numbers, $0 < Ca \leq 20$, where $Ca = \mu U/\sigma$; μ is the dynamic viscosity of the liquid, U is the surface velocity of the inner rotating cylinder, and σ is the coefficient of surface tension. These conditions include cases in which the free surface is nearly flat at small Ca up to highly deformed at large Ca. While the capillary number is a ratio of interfacial to viscous forces, we note that the large scale flow is determined primarily by a balance of viscous and gravity forces. At small Ca in a half-filled annulus the flow consists of two cells, delineated by a separatrix. One cell orbits the rotating cylinder: it is this feature which clearly differentiates the actual physical flow from the mathematical analysis of [4] and [6].

The structure of the flow implies the need for a stagnation line and a cusp line [7] at the free surface. The cusp line eventually deforms the free surface rather extremely as Ca grows, with the radius of curvature expected [8] to be proportional to $\exp(-\beta Ca)$ once $Ca \gtrsim 1$, where β is a contant. At sufficiently large rotation rate, *i.e.* large Ca, the cusp becomes unstable [9] and air entrainment is observed [10].

Motivation for study of this annular free surface flow arises from phenomena first seen in its application in bioreactors. In this application, a suspension of biological cells is made and fills the annular region, with the flow driven by rotation of the inner cylinder both maintaining cell suspension and enhancing mass transfer of oxygen from the free surface into the bulk. In addition, however, it was observed that the cells formed bands of high and low concentration alternating along the axis of the cylinder, and this has been followed by a number of studies of simpler rigid-particle suspensions [11] and the related flow in a single partially filled cylinder [12–16]. In these studies, the concentration of solids is found to vary axially in alternating bands, with solid fraction even approaching zero in some cases, for $F = 0.5$–0.95 [11,17]. For the single-cylinder flow, an explanation for the banding process that occurs within a partially filled horizontal rotating cylinder has been proposed [18] based on a lubrication approximation for the flow [19] applied in an analysis for a suspension having a particle-concentration–dependent effective viscosity. The banding instability in the partially filled Couette has been suggested to be mechanistically related to differential drainage rates between particles and fluid [20], and these ideas have been developed into a predictive model [17]. Such analysis has been hampered, because the flow complexity within this geometry does not allow for effective analytical treatments of the global flow. To allow further progress in understanding such flows in application and analysis of multiphase phenomena, we consider the flow with the partially filled Couette in detail.

As this flow is rather complex, it is of interest to develop understanding using numerical tools in combination with experiments. We apply a phase-field model, a diffuse-interface approach, in order to compute the flow over a wide range of conditions and compare against the experiments. We begin in sect. 2 with a description of the experimental setup. The numerical method is presented in sect. 3. A comparison between experimental and numerical results is provided in sect. 4.

2 Experimental setup

Experiments were performed within concentric cylinders shown schematically in fig. 1(a). The outer cylinder is a transparent tube made of acrylic and the interior cylinder is stainless steel. The annulus is closed at each end by acrylic caps into which a sealed bearing is mounted, allowing the inner cylinder to turn while the caps and the outer cylinder are stationary. The device is mounted horizontally, its length is $L = 304 \pm 0.1$ mm and measurements are performed at $L/2$ from the caps (*i.e.*, at the middle). Specifically, high resolution images of liquid levels and film thickness at different rotation speeds were compared and sized using image processing softwares (MATLAB and ImageJ). Several calibrations were performed and all the data are reported with their associated error bars.

Figure 1(b) shows a sketch of the cross-sectional view of the setup where $R_i = 9.5 \pm 0.1$ mm and $R_o = 22 \pm 0.2$ mm. The gap width is $d = R_o - R_i = 12.5$ mm, and the radius ratio is $R_i/R_o = 0.43$, which is normally termed a wide-gap Couette geometry. The cylinder motion is motor-driven (Dayton; model 1L497) and the angular velocity of the inner cylinder can be varied from $\omega \simeq 1$ to 42 rpm, so $U = 2\pi\omega R_i \simeq 1$ to 42 mm/s. Figure 1(b) sketches a cross-sectional view of the liquid film around the inner cylinder. Once the inner cylinder rotates, it drags out a liquid film on one side, and this film then reenters the liquid pool in the annulus on the other side.

The liquid used in the experiments is lubricant UCON 75-H-90,000 (Dow Chemical) of density 1092 kg/m^3 and surface tension 35–40 mN/m at 20°C. This lubricant is stable, noncorrosive, water soluble and its contact angle with acrylic in air is 70–90 degrees. The dynamic viscosity of the liquid was determined from shear ramps of increasing

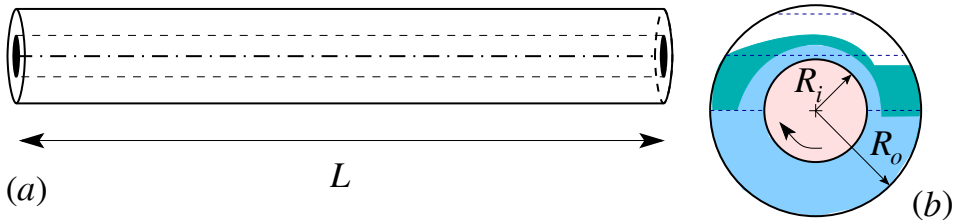

Fig. 1. (Color online) Schematic of the experimental setup. (a) Horizontal concentric cylinders, drawn to scale. (b) Cross-sectional view: a liquid film is coating the inner cylinder. The lighter color represents the liquid in a 50% full annulus, the darker color represents the case of 75% full annulus, both under flow; the dashed horizontal lines represent the levels for 50%, 75% and 90% filling levels (from bottom to top) in the absence of flow.

and decreasing shear rate using a cone-and-plane geometry in a rheometer (TA Instruments). The viscosity is sensitive to temperature, so the room temperature variations are taken into account. The viscosity, μ, in the range 15 to 35°C, can be represented by $\mu(T) = A\exp(-E/RT)$, with $A = 94.35\,\mathrm{Pa\,s}$ and $E = 0.95\,\mathrm{J\,mol^{-1}}$; here T is in Kelvin, and $R = 8.314\,\mathrm{J\,K^{-1}\,mol^{-1}}$ is the gas constant.

We identify five dimensionless parameters describing the flow: a) the Reynolds number which is defined as $Re = UR_i/\nu = 2\pi\omega R_i^2/\nu$; b) the ratio of the inner to outer radius of the annulus; c) the Bond number $Bo = \rho g R_i^2/\sigma$; d) the fill fraction F, *i.e.* ratio between the liquid volume and the annular gap volume between the two cylinders; and e) Ca as defined above. Since $Re = UR_i/\nu = O(10^{-3}$–$0.1)$, inertia may safely be neglected. Indeed, in a similar configuration at filling fraction 0.66 and a thin gap width with radius ratio 0.882, the authors of [21] found that the flow is unstable to inclined traveling rolls from $Re \approx 250$.

With Re essentially zero, a fixed radius ratio (0.43), and constant Bo (28), the independently variable parameters are reduced to two, namely F and Ca. We note that an alternative way of expressing the dimensionless parameters would be to take the ratio between viscous and gravitational forces (which is physically related to the drainage from the cylinder) defined as $\alpha^2 = \omega\nu/gR_i$, where g is the gravitational acceleration. As an alternative, one may use $\alpha^2 = 0.032\,Ca$ for the work described here, and thus $\alpha^2 = O(0.001$–$1)$. We prefer to use the ratio between viscosity and capillary forces captured in Ca, as the free surface here exhibits a cusp. One may view Ca as a convenient nondimensionalization of U on large scales, while retaining the interpretation as a viscous-capillary balance at small feature scales.

3 Numerical formulation

This flow is modeled as axially invariant, and thus we reduce to a two-dimensional calculation on a cross-section. We compute the flow based on the Navier-Stokes equations including a surface tension term

$$\nabla\cdot\mathbf{u} = 0, \tag{1}$$

$$\rho\frac{\partial\mathbf{u}}{\partial t} + \rho\mathbf{u}\cdot\nabla\mathbf{u} = -\nabla p + \mu\nabla\cdot\mathbf{D} + \rho\mathbf{g} + G\nabla\phi, \tag{2}$$

where $\mathbf{u}$ is the velocity, $\mathbf{D}$ is the strain rate tensor: $\mathbf{D} = \nabla\mathbf{u} + (\nabla\mathbf{u})^T$, ρ is the fluid density, t is time, p is the pressure, $\mathbf{g}$ is the gravity, and the last term of eq. (2) represents the surface tension force with G the chemical potential ($\mathrm{J/m^3}$) and ϕ the phase-field variable. We note that $-1 \le \phi \le 1$.

The surface tension is obtained from the Cahn-Hilliard equation, which is given by

$$\frac{\partial\phi}{\partial t} + \mathbf{u}\cdot\nabla\phi = \nabla\cdot\frac{\gamma\lambda}{\epsilon^2}\nabla\psi, \tag{3}$$

where ψ is an auxiliary variable satisfying

$$\psi = -\nabla\cdot\epsilon^2\nabla\phi + \left(\phi^2 - 1\right)\phi + \frac{\epsilon^2}{\lambda}\frac{\partial f}{\partial\phi}, \tag{4}$$

where f is the free energy, γ is a mobility with a fixed value for our work ($\gamma = 10\,\mathrm{m^3\,s/kg}$), λ is the mixing energy density, and ϵ is the interface thickness scale. Note that $\epsilon = 10^{-4}\,\mathrm{m}$ is also constant. It is assumed that the diffuse interface is at equilibrium and thus $\partial f/\partial\phi = 0$. There is a relation [22] between λ, ϵ and the surface tension coefficient such that $\sigma \propto \lambda/\epsilon$, and the chemical potential is defined as $G = \lambda\psi/\epsilon^2$. While boundary element approaches [7, 23–25] are likely to be able to more accurately resolve the detailed structure near the cusp because it reduces the dimensionality of the calculation (here, to the surface contour), this requires an additional step in determining the flow field. For the determination of flow field structure of interest here, the diffuse-interface approach on a spatially variable-mesh density is an efficient and satisfactory method.

We simulate the evolution of $\mathbf{u}$ and ϕ in time using a finite element solver (COMSOL Multiphysics). The geometry described in sect. 2 is implemented in a two-dimensional cylindrical coordinate system. Equations (1)–(4) combined with the no-slip boundary condition at the outer cylinder and oil initially wetting the inner rotating cylinder are solved for small Re. The finite element solver also allows for calculations with a level-set method. However the phase-field method was chosen because it can be constructed by physical arguments and is often used to model viscous flows. In the calculation results presented here, all input parameters equal to the parameters stated in the experimental section, with the upper fluid being air with viscosity $1.73\times10^{-5}\,\mathrm{Pa\,s}$.

The contact angle between the oil and the outer wall can be varied as a boundary condition. This influences the shape of the interface close to the outer wall, the stagnation point position and the cusp position. In the results presented here the contact angle is fixed to 90 degrees. The calculations are unsteady. In any calculation reported, after sufficient time steps a steady solution is observed and the asymptotically steady solution is presented here. The total number of elements of the two-dimensional mesh varies with F and is over 40 000 elements. As noted, the mesh density is also spatially variable within a calculation, and a very fine mesh is used along the interface, particularly near the cusp, as well as along the inner and outer surfaces.

4 Results and discussion

We first describe the experimental measurements and the calculations as a function of Ca for the half-full case, *i.e.* $F = 0.5$. We present results for the film thickness, cusp angle and stagnation line radial position. From these measurements, the shape of the free surface is reconstructed, and its deformation is compared to numerical calculations. For $F = 0.75$, the comparison between experiments and calculations is presented. The results for $F = 0.9$ indicate the presence of a single flow cell.

4.1 Half-full case: F = 0.5

4.1.1 Film thickness

Each experiment began with the apparatus carefully positioned with axis horizontal, and the annulus was filled to the desired fill level with the viscous liquid. The inner cylinder rotation was then started at the desired rate. As noted, this cylinder motion drags a film over the cylinder and into the liquid pool. Hence, the flow consists of two cells, each extending the full range of possible wetted angles around the cylinder. A drawing of a cross-sectional view of the flow pattern is provided in the inset of fig. 2.

Turning to quantitative results, we first consider the film thickness over the inner cylinder, h. As the rotation rate increases, the film thickness increases and the reduction in liquid level downstream, denoted H, also grows as indicated in fig. 2. The error bars represent the spread around an average, taken from two to four measurements. Note that the measured h is roughly proportional to $Ca^{0.46}$ which is consistent with the theoretical scaling of $h \sim Ca^{0.5}$ for the thickness of a liquid film on a vertical flat plate being pulled from an infinite bath for $Ca \gtrsim 1$ [26–28]. Interestingly, the downstream surface level reduction, H, evolves similarly to h for small rotation rates, but appears to saturate within error bar while h continues to grow; specifically, for $Ca \gtrsim 4$, H tends toward a constant value. The saturation before interface breakup may be due to three-dimensional effects or transversal flow [29]. The scatter on the measured H is

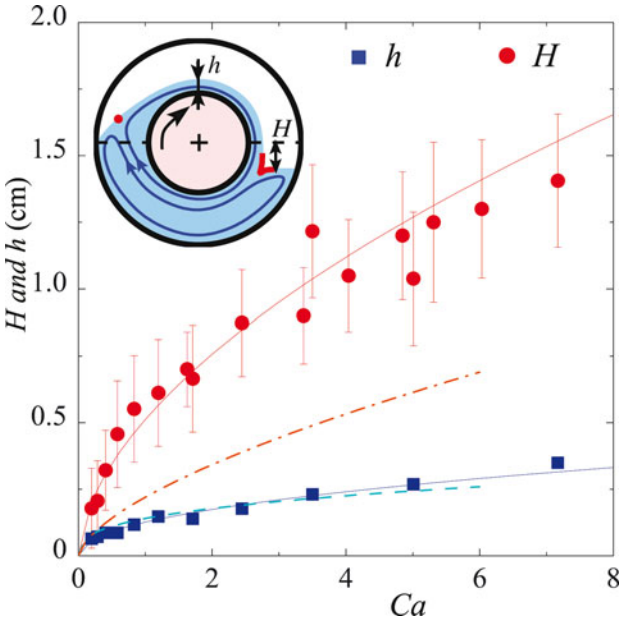

Fig. 2. (Color online) Film thickness, h, and downstream surface level reduction, H, as a function of Ca for the half-full apparatus. The continuous lines represent $H = 0.51\ Ca^{0.56}$ and $h = 0.13\ Ca^{0.46}$ (H and h are expressed in cm). The dashed lines represent the numerical results. The inset sketches the cross-section flow pattern as well as h, H, the stagnation point (red dot) and the cusp.

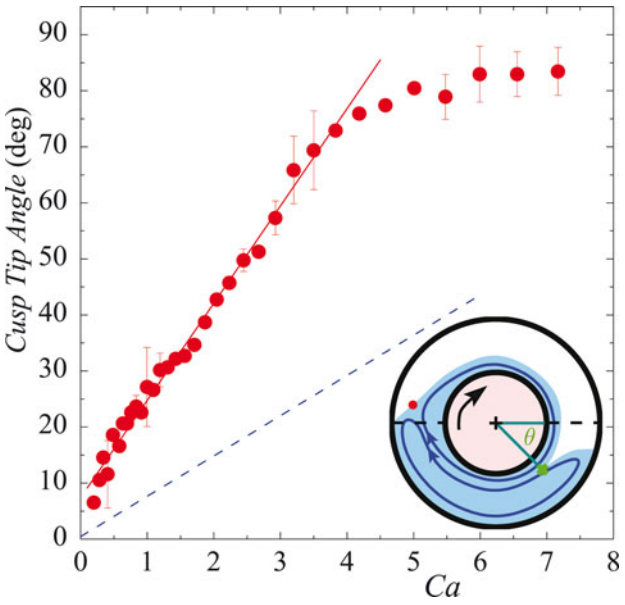

Fig. 3. (Color online) Angle of the cusp tip, θ, as a function of Ca for the half-full apparatus. The continuous line represents a linear fit: $\theta \propto Ca$. The dashed line represents the numerical results. The inset sketches the cross-section flow pattern as well as θ and the stagnation point (red dot).

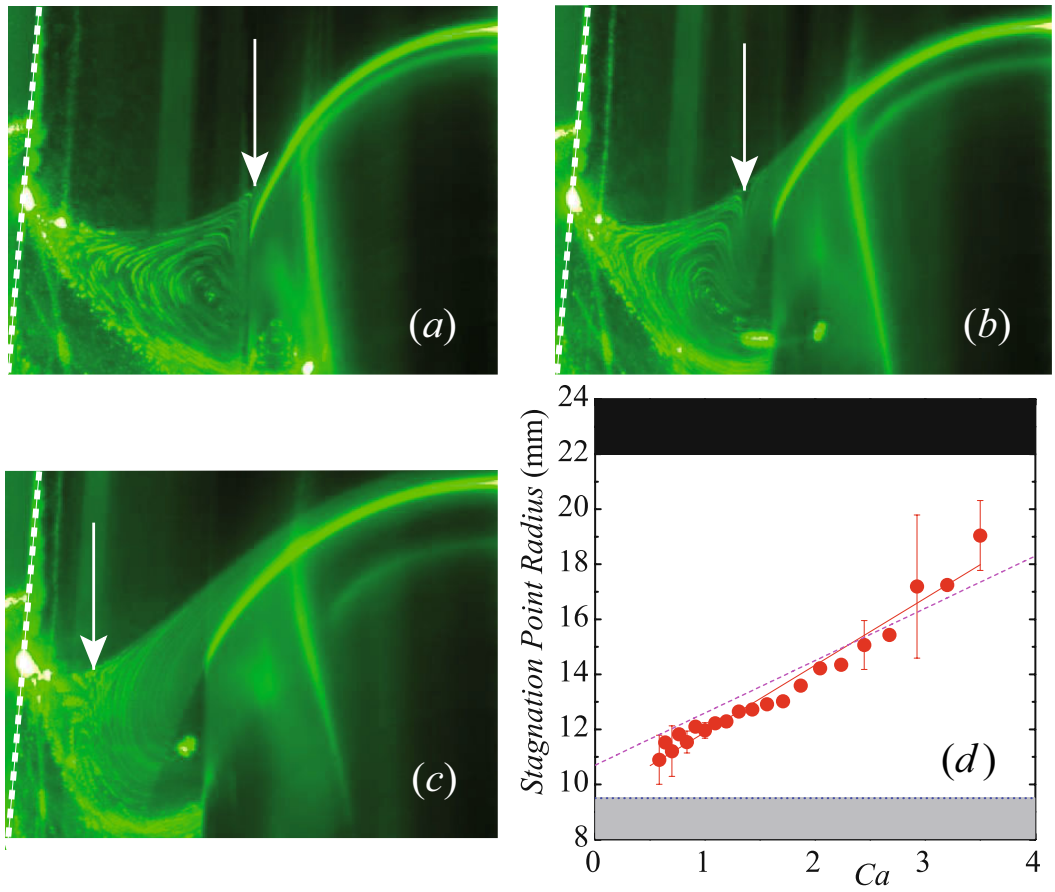

Fig. 4. (Color online) Time lapse photographs of the cross-section in the rising side of the rotating cylinder: (a) $Ca = 0.4$, (b) $Ca = 1.7$, and (c) $Ca = 3.5$ for $F = 0.5$. The white arrow indicates the position of the stagnation line. The dashed white line on the left of each photograph indicates the outer wall position and the right side of each picture is in the vertical plane passing through the rotating axis of the inner cylinder, which is rotating in the clockwise direction. (d) Radial position from the cylinders axis of the stagnation line as a function of Ca. The continuous line represents a linear fit: $2.4\,Ca + 9.6$ (expressed in mm), with the inner cylinder radius: $R_i = 9.6$ mm. The dashed line represents a fit of the numerical results.

large because of complications associated with the dynamics of the contact line at the outer cylinder surface. The predictions from the numerical solution are also shown in fig. 2, and are in good agreement with the measurements for h, in fact lying within the experimental error. The predicted H underestimates the measurements.

4.1.2 Cusp angle

On the downstream side of the rotating cylinder, a viscous cusp is formed as in related experiments by [7,8,30]. Whereas these previous studies consider a large pool, here the confinement or the radius ratio affects the cusp tip position. For sufficiently high Ca, the angular position of the cusp tip relative to the original flat interface, θ, was determined, as sketched in the inset in fig. 3. The evolution is roughly linear for $Ca < 4$, but reaches a limiting value of $\theta = 86 \pm 4°$. In the range $Ca \leq 4$, the experimental data can be described with a linear fit, $\theta = 17.4\,Ca + 7.4$. Note that the fit does not predict zero for the origin because the detection of a cusp at low Ca is not straightforward, but we note the slope is somewhat larger for $Ca < 1$. The evolution of the tip radius has been described in related configurations [8,30] and it has been found that the radius of curvature, r, is proportional to $\exp(-\beta Ca)$ when $Ca \gtrsim 1$. As expected the numerical data predict an exponential decrease ($r = 2.78\exp(-0.28Ca)$) of the radius of curvature of the cusp as a function of Ca for $1 \leq Ca \leq 6$.

The calculations results for the tip angle are also reported in fig. 3. Again the model is in qualitative agreement with the experiments, but underestimates θ. The simulation does not recover the saturation region; this could be due to three-dimensional effects not captured in the calculations.

The cusp is asymmetric, as the velocity in the cell adjacent to the inner cylinder is about one order of magnitude larger than that in the outer recirculation cell. The calculations predict the interface breakup and air entrainment at the cusp for $Ca_c \simeq 6$ whereas it is $Ca_c \simeq 8$ in the present experiment. This critical velocity or Ca_c is in agreement with previous measurements [30] where a scaling of Ca_c as a function of the viscosity ratio of the two

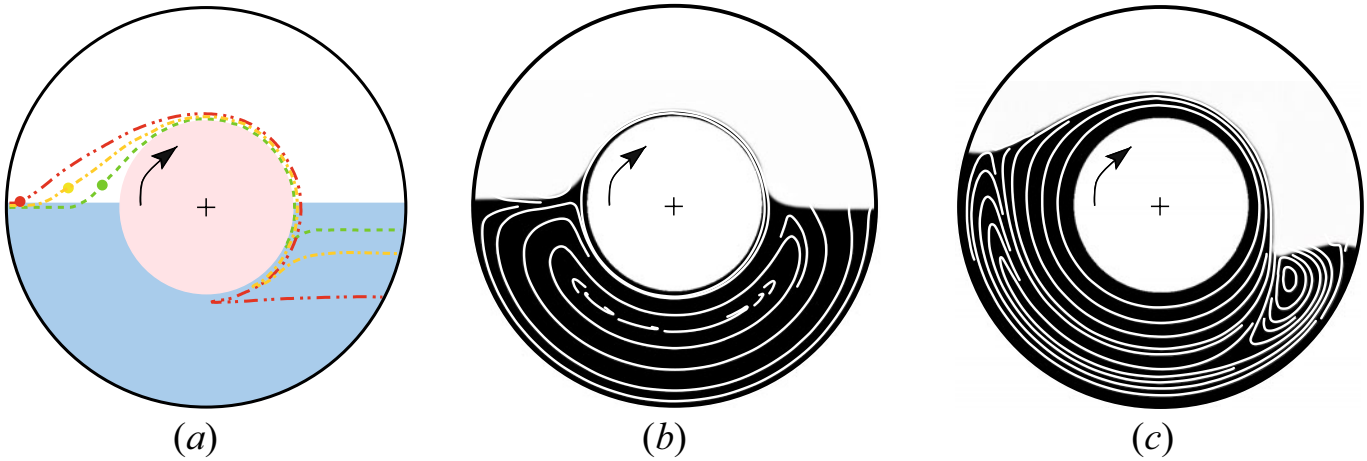

Fig. 5. (Color online) (a) Reconstruction of the free surface at $F = 0.5$ in the absence of flow (light blue filled region), $Ca = 1$ (dashed green line), $Ca = 3$ (dashed-dotted yellow line), and $Ca = 6$ (dashed-dotted-dotted red line). The stagnation line positions are represented by filled dots. (b) and (c) Numerical simulation of the flow for $Ca = 0.9$ and 3.7, respectively. The white lines are velocity streamlines.

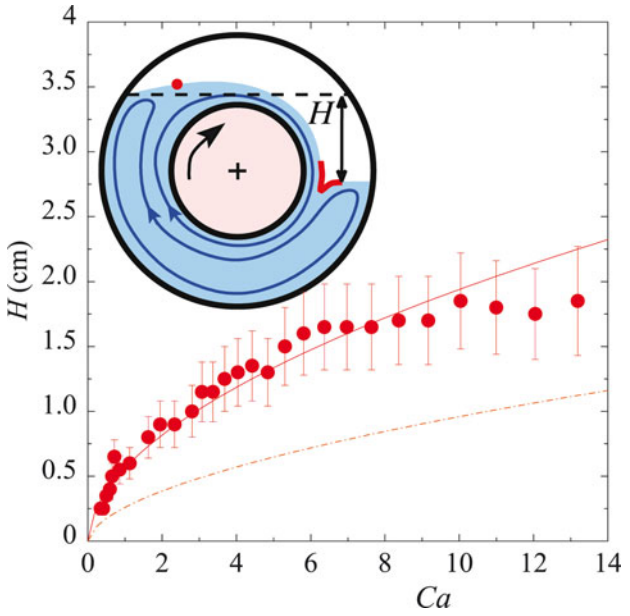

Fig. 6. (Color online) Downstream surface level reduction, H, as a function of Ca for $F = 0.75$. The line represents $H = 0.56\ Ca^{0.54}$ (expressed in cm). The dashed line represents a fit of the numerical results. The inset sketches the cross-section flow pattern as well as H and the stagnation point (red dot).

fluids is observed in agreement with an exponent of $-4/3$ proposed by Eggers [31].

4.1.3 Stagnation line position

Between the two large cells on the rising side of the inner cylinder, there is a stagnation line on the free surface where close streamlines separate. Using time lapse photography and a dilute seeding with 50 μm diameter polyamide particles (from Dantec), the cells can be observed, as depicted in the photographs of fig. 4. A laser sheet is generated perpendicular to the cylinder axis and photographs are taken at an angle of 30° from the horizontal. Quantitative positions of the stagnation line are extracted by comparison with the initial static liquid level. The radial position of the stagnation line increases linearly with Ca as indicated in fig. 4(d). Note that for small Ca, the stagnation line is on the surface rising over the inner cylinder. As Ca increases, the stagnation line moves along the free surface towards the outer wall, while there is a rise and change in curvature of the free surface. As the stagnation line closely approaches the stationary wall, the secondary cell weakens and we are unable to resolve it on the rising side of the rotating cylinder for $Ca > 3.5$. The calculations of the flow reproduce the linear evolution of the stagnation line position within experimental error. We could not experimentally access the limit $Ca \to 0$, but in this limit (obtained by taking $U \to 0$) the stagnation point is expected to asymptotically approach the inner cylinder surface as the film thickness tends to zero; the linear fit of the stagnation point radial position, $2.4\ Ca + 9.6$ (expressed in mm), with the inner cylinder radius $R_i = 9.6$ mm, is in good agreement with this expectation.

The finding that the cusp angle, θ, and the surface level reduction, H, both approach limiting values for $Ca > 4$ suggests there is a roughly fixed flow structure, with the position of the secondary cell underneath the rotating cylinder and the primarily cell varying little as the rate increases. However, h continues to grow with increasing rotation rate.

The numerically computed flow is quantitatively in agreement in terms of the position of the stagnation line and h. The evolution of H and θ as a function of Ca is only qualitatively predicted. A number of runs have been carried out varying the contact angle at the outer wall from 30 to 150 degrees and small changes on the film thicknesses

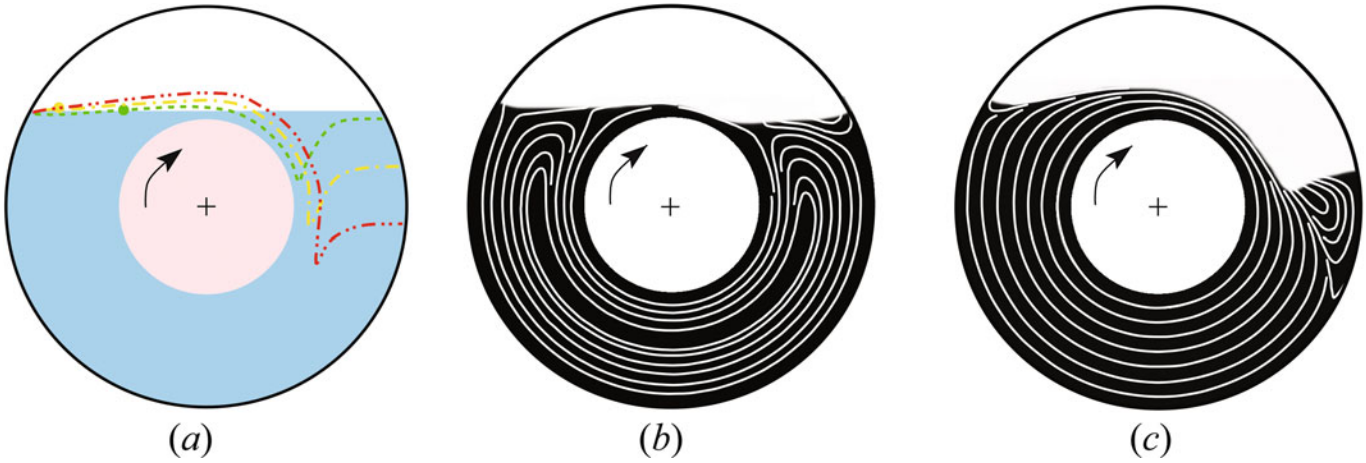

Fig. 7. (Color online) (a) Reconstruction of the $F = 0.75$ free surface for no flow (light blue filled region), $Ca = 1$ (dashed green line), $Ca = 3$ (dashed-dotted yellow line), and $Ca = 6$ (dashed-dotted-dotted red line). The stagnation lines positions are represented by filled dots. Note that there is no dot on the upper left side for $Ca = 6$. Numerical calculations for (b) $Ca = 0.1$ and (c) $Ca = 3.7$ where the secondary cell is confined to the right corner. The white lines are velocity streamlines.

and the positions of the cusp were observed. The main effect of the contact angle is the curvature of the interface close to the outer wall. So our present understanding is that the contact angle is not the only responsible for the discrepancy between experiments and numerical results.

4.1.4 Free surface morphology

From the experimental measurements of film thickness, downstream surface level reduction, cusp angle, and the radial position of the stagnation line, we reconstruct the free surface. We assume that the contact line on the rising side is pinned at the wall because observations indicate it does not change with Ca. Figure 5(a) presents a reconstruction of the free surface for $F = 0.5$. Note that the surface on the downstream side of the inner cylinder is dropped in elevation compared to the initial condition by H, providing the liquid volume associated with the film and the free surface rise around the stagnation line region. The output of the numerical simulation is also displayed in fig. 5(b) and (c), with results at $Ca = 0.9$ and 3.7, respectively. The free surface as well as numerical streamlines for the bottom fluids are also reported. As Ca increases, the two cells become more asymmetric about the vertical centerline. The upper cell in which the flow orbits the inner cylinder grows, as does the film which forms a part of this cell.

4.2 3/4 full case: F = 0.75

4.2.1 Film thickness

When the annulus is 3/4 full, the film thickness, h, has a finite value of approximately 1 mm at $Ca = 0$ (no flow) and increases with Ca. The variation of h is represented by $h \propto Ca^{0.5}$ in the range $2 < Ca < 5$. Meanwhile, the reduction in liquid level downstream surface level, H, again varies roughly as $Ca^{0.5}$ in the range $2 < Ca < 5$ as depicted in fig. 6.

4.2.2 Free surface morphology

For $F = 0.75$, the reconstruction of the free surface from measurements is depicted on fig. 7(a). As explained earlier, the stagnation line moves toward the stationary wall as Ca increases. From the numerical calculations, we find that for small Ca, there are two counter-rotating cells and the stagnation line moves along the free surface toward the outer wall with increasing Ca. The cusp penetration depth is only a few millimeters below the level of the annular pool surface, *i.e.* the surface defining H. Moreover, the cusp does not go unstable to breakup even for large rotation speed corresponding to $Ca = 20$.

Figures 7(b) and (c) present the results of calculations for $Ca = 0.1$ and 3.7, respectively. For small Ca, the flow pattern consists of two cells almost symmetric with respect to the vertical axis. As Ca increases, the bottom cell reduces in size and at large Ca, the outer cell gets confined on the cusp side along the outer cylinder. As Ca increases, the cell reduces in size and eventually disappears.

4.3 Effect of the filling ratio, F

Experiments were conducted for $F = 0.9$. Only a single cell around the inner cylinder is observed for this large fill fraction. There is apparently a continuous transition in the flow structure between $F = 0.75$ (where two cells appear at small Ca) and $F = 0.90$ with its single cell. Note that this behavior is specific to the experimental geometry studied here, with $R_i/R_o = 0.43$.

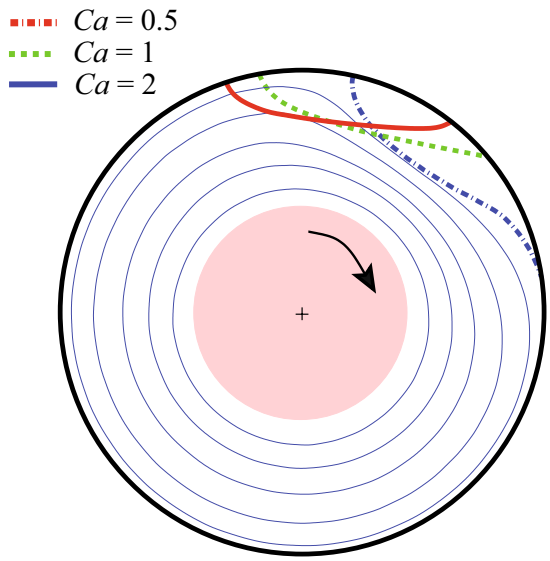

Fig. 8. (Color online) Numerical calculations for $F = 0.90$ and $Ca = 0.5$, 1 and 2. The thick lines represent the interfaces and the thin lines represent velocity streamline in the viscous liquid for the case $Ca = 2$, which evidence only a single cell.

In fig. 8, results of calculations for $F = 0.9$ for $Ca = 0.5$, 1 and 2 are presented. Below $Ca = 0.5$, the interface is almost symmetric with respect to the vertical axis. As Ca increases, the interface deforms and the positions of the contact lines move. Although there is a significant interface deformation, the streamlines of the liquid flow form only a single circulation cell. At high Ca, no cusp can be detected, and the effect of rotation rate leads to minimal changes in the position of the free surface even for large rotation speeds corresponding to $Ca = 20$.

The agreement between our experiments and the calculations leads to the following conclusions. For $F = 0.5$, two cells are always observed up to cylinder rotation rates which cause interface breakup. For $F = 0.75$, there is a transition from two cells to a single cell for Ca between 2 and 3. For $F = 0.9$, only a single cell is observed.

5 Summary

The present work provides information necessary for understanding of the flow in the neighborhood and at the free surface of flow in a partially filled horizontal Couette device, and could serve as the basis for application of the flow or to support analysis of the flow-induced segregation in the particle-laden flow in the same geometry. In addition, the results serve as an interesting test of the accuracy of numerics of free-surface Stokes flow as this flow exhibits features on a range of scales from the cusp to the global structure, as well as a very rich sub-surface flow topology.

Specifically, we have quantified the morphology of the free surface of the flow of a very viscous liquid in a partially filled Couette apparatus at annular filling fractions of $F = 0.5$, 0.75, and 0.9. When the inner cylinder rotates, a thin liquid film is dragged over and plunged into the remaining liquid pool. At the smallest F, two counter-rotating flow cells are observed, one directly adjacent to, and driven by the motion of, the inner cylinder and the other a recirculation lying below. At the free surface, these flow zones are delimited by a stagnation line and a cusp line. When increasing the flow rate, the stagnation line moves from the inner cylinder to the steady wall. On the downstream side of the rotating cylinder, the tip of the cusp line moves below the inner cylinder as the rotation rate increases, with significant deformation of the cells. At the intermediate fill fraction of $F = 0.75$, a significant decrease in size of the bottom cell with increasing rotation rate is found, while $F = 0.9$ exhibits only a single cell for all driving rates.

To properly understand the phenomena in this free-surface Couette geometry and related systems requires consideration of the free surface structure as a function of dynamical variables. The quantitative reconstruction of the free surface, confirmed by our calculations of the flow, indicates that the deformation at elevated driving rates is extreme for the lower fill fractions. A comparison between the measurements and these calculations using a phase-field (diffuse interface) model of the free surface is provided. The position of the stagnation line and the height of the liquid film over the inner cylinder are quantitatively predicted. However, the position of the cusp and the liquid level downstream are only qualitatively recovered by the calculations.

Partial funding for this research (support of P. Mirbod) was provided by the CCNY/UofChicago MRSEC Partnership on the Dynamics of Heterogeneous and Particulate Materials, an NSF PREM (DMR-0934206), and partial funding (software, supplies, and support of J. Morris and P. Mirbod) was provided by the donors of the ACS Petroleum Research Fund (49080-ND9). The authors are grateful to Coralie Carmouze, John Coulet, and Lukas Schimmer for assistance in the initial experiments. We also acknowledge Andreas Acrivos for comments on our earlier version of the paper.

References

1. R.T. Balmer, Nature **227**, 600 (1970).
2. S.T. Thoroddsen, L. Mahadevan, Exp. Fluids **23**, 1 (1997).
3. F. Melo, S. Douady, Phys. Rev. Lett. **71**, 3283 (1993).
4. M.C.T. Wilson, P.H. Gaskell, M.D. Savage, Phys. Fluids **17**, 093601 (2005).
5. M. Brøns, Adv. Appl. Mech. **41**, 1 (2007).
6. P.H. Gaskell, M.D. Savage, M. Wilson, J. Fluid Mech. **337**, 263 (1997).
7. D.D. Joseph, J. Nelson, J. Renardy, Y. Renardy, J. Fluid Mech. **223**, 383 (1991).
8. J.-T. Jeong, H.K. Moffatt, J. Fluid Mech. **241**, 1 (1992).
9. Y.C. Severtson, C.K. Aidun, J. Fluid Mech. **312**, 173 (1996).
10. K.T. Kiger, J.H. Duncan, Annu. Rev. Fluid Mech. **44**, 563 (2012).
11. M. Tirumkudulu, A. Tripathi, A. Acrivos, Phys. Fluids **11**, 507 (1999).

12. M.J. Karweit, S. Corrsin, Phys. Fluids **18**, 111 (1975).
13. O.A.M. Boote, P.J. Thomas, Phys. Fluids **11**, 2020 (1999).
14. M. Tirumkudulu, A. Mileo, A. Acrivos, Phys. Fluids **12**, 1615 (2000).
15. P.J. Thomas, G.D. Riddell, S. Kooner, G.P. King, Phys. Fluids. **13**, 2720 (2001).
16. E. Guyez, P.J. Thomas, Phys. Fluids. **21**, 033301 (2009).
17. B.D. Timberlake, J.F. Morris, Philos. Trans. R. Soc. A **361**, 895 (2003).
18. B. Jin, A. Acrivos, Phys. Fluids **16**, 641 (2004).
19. M. Tirumkudulu, A. Acrivos, Phys. Fluids **13**, 14 (2000).
20. B.D. Timberlake, J.F. Morris, Phys. Fluids **14**, 1580 (2002).
21. I. Mutabazi, J.J. Hegseth, C.D. Andereck, J.E. Wesfreid, Phys. Rev. A **38**, 4752 (1988).
22. P. Yue, J.J. Feng, C. Liu, J. Shen, J. Fluid Mech. **515**, 293 (2004).
23. M.K. Berkenbush, I. Cohen, W.W. Zhang, J. Fluid Mech. **613**, 171 (2008).
24. J. Eggers, S. Courrech du Pont, Phys. Rev. E **79**, 066311 (2009).
25. D. Zhou, J.J. Feng, J. Non-Newtonian Fluid Mech. **165**, 839 (2010).
26. S.D.R. Wilson, J. Engg. Math. **16**, 209 (1982).
27. P.-G. de Gennes, F. Brochard-Wyard, D. Quéré, *Gouttes, bulles, perles et ondes* (Editions Belin, 2002).
28. B. Jin, A. Acrivos, A. Munch, Phys. Fluids **17**, 103603 (2005).
29. G. Bohme, G. Pokriefke, A. Muller, Arch. Appl. Mech. **75**, 619 (2006).
30. E. Lorenceau, F. Restagno, D. Quéré, Phys. Rev. Lett. **90**, 184501 (2003).
31. J. Eggers, Phys. Rev. Lett. **86**, 4290 (2001).